



Research Paper

Cite this article: Rusanen J, Sethi A, Tervo N, Kiuru V, Rahkonen T, Pärssinen A, Aikio JP (2024) Ka-band stacked and pseudo-differential orthogonal load-modulated balanced power amplifier in 22 nm CMOS FDSOI. *International Journal of Microwave and Wireless Technologies* **16**(5), 763–770. <https://doi.org/10.1017/S1759078723001137>

Received: 02 June 2023
Revised: 13 september 2023
Accepted: 18 september 2023

Keywords:

active matching; fifth generation (5G); fully depleted silicon-on-insulator (FDSOI); millimeter-wave (mmWave); power amplifier; stacked power amplifier

Corresponding author: Jere Rusanen;
Email: jere.rusanen@oulu.fi

Ka-band stacked and pseudo-differential orthogonal load-modulated balanced power amplifier in 22 nm CMOS FDSOI

Jere Rusanen , Alok Sethi, Nuutti Tervo, Veeti Kiuru, Timo Rahkonen, Aarno Pärssinen and Janne P. Aikio

Faculty of Information Technology and Electrical Engineering, University of Oulu, Oulu, Finland

Abstract

This paper presents an integrated power amplifier (PA) following the orthogonal load-modulated balanced amplifier (OLMBA) topology. The fixed-phase prototype in this paper is implemented with 22 nm complementary metal oxide semiconductor (CMOS) fully depleted silicon-on-insulator (FDSOI) process. The proposed PA operates at 26 GHz frequency range, where it achieves 19.5 dBm output power, 16.6 dB gain, 15.7% power added efficiency, and 18.3 dBm output 1-dB compression point ($P_{1\text{dB}}$). The PA is also tested with high dynamic range modulated signals, and it achieves, respectively, 11.4 dBm and 4.9 dBm average output power (P_{avg}) with 100 MHz and 400 MHz 64-QAM third-generation partnership project/new radio frequency range 2 signals, and 14 dBm P_{avg} with 0.6 Gb/s (120 MHz) single carrier 64-QAM signal, measured at 26 GHz and using -28 dBc adjacent channel leakage ratio and -21.9 dB (8%) error vector magnitude as threshold values. The proposed OLMBA is also compared to a stand-alone quadrature-balanced PA. Modulated measurements show that the stand-alone quadrature-balanced PA has better linearity in deep back-off, but the OLMBA has better efficiency.

Introduction

Fifth generation (5G) and the forthcoming sixth generation (6G) networks aim to provide higher data rates and reliable, low latency, and power-efficient wireless networks [1–4]. In order to achieve these goals, third generation partnership project (3GPP) new radio (NR) standard allocates several wideband millimeter-wave (mmWave) frequency bands between 24 and 71 GHz [5]. In order to compensate for increasing path losses, large phased arrays with multiple antenna elements and RF beamformer at mmWave frequency range are proposed [6–8]. Indeed, link analysis indicates the need for excessive antenna gain [9, 10]. As a result, mmWave transceivers require small-form factor front-end circuitry due to the physically tight antenna spacing. When the number of active antenna terminals increases, less power from a single power amplifier (PA) is needed and therefore compact, silicon-based PAs become a feasible option [11, 12]. In contrast to the lower frequency PAs, integrated mmWave PAs cannot be easily linearized with digital pre-distorter due to the wide modulation bandwidths and a large number of parallel PAs to be linearized [13]. As a result, research has been ongoing for years to seek out suitable PA solutions for mmWave transmitters [14–22].

In order to achieve high efficiency, Doherty load modulation PA has been popular [22, 23]. Besides Doherty, a recent technique for active load tuning called load-modulated balanced amplifier (LMBA) has been proposed, and integrated mmWave implementations already exist [24–26]. In the LMBA technique, the RF control signal is injected in the isolation port of the output quadrature coupler and the balanced PA pair experiences symmetric load modulation. Since the load modulating signal is injected on the output side, it needs to be roughly the same magnitude as the primary PA outputs in order to vary the load. On the other hand, the control signal can add to the total output power. Recently, LMBA has further evolved into an orthogonal load-modulated balanced amplifier (OLMBA) [27]. In OLMBA, control signal is injected into the isolation port of the input quadrature coupler and the reactive load at the output quadrature coupler reflects the control signal back to the balanced PA pair outputs, resulting in load modulation. The load seen by the balanced amplifier pair, therefore, depends on the phase and amplitude of the control signal, as well as the reactive load. The advantage of OLMBA is the fact that the control signal can be weak, as it is amplified by the balanced amplifier pair. In addition, OLMBA load modulation is asymmetric by default. Asymmetric load modulation can be beneficial for example in load-pull mitigation [28].

© The Author(s), 2023. Published by Cambridge University Press in association with the European Microwave Association. This is an Open Access article, distributed under the terms of the Creative Commons Attribution licence (<http://creativecommons.org/licenses/by/4.0>), which permits unrestricted re-use, distribution and reproduction, provided the original article is properly cited.

This paper is an extension of [29], which presented, to the authors' best knowledge, the first fully integrated OLMBA, designed and fabricated using GlobalFoundries 22 nm fully depleted silicon-on-insulator (FDSOI) [30]. The following sections provide the design overview of a fixed-phase prototype OLMBA, followed by extensive measurements featuring high dynamic range 5G signals. This extended version is thoroughly revised, provides a more detailed look into design theory, and presents additional measurement results comparing the performance with stand-alone quadrature-balanced PA.

Design

The integrated OLMBA implementation in this paper (Fig. 1) comprises four PA blocks and three quadrature hybrids. The output stage contains two PAs (BA1 and BA2) and the driving stage consists of the main driver amplifier (DR) and load modulating control amplifier (CA). All of the building blocks are matched to 50 Ω. The benefit of the 50 Ω-matched block approach is simplicity since all the building blocks in the line-up can be designed and treated as separate entities. The disadvantage to this approach is the increased amount of intermediate matching, along with the losses and area costs involved.

PA block

Starting point of the PA design was a 75-μm-wide three-stacked power cell containing also the upper gate capacitors needed for even voltage distribution among the stacked transistors. The stacking enabled increasing the drain bias voltage up to 2.7 V. The main signal driver (DR) and the PA pair forming the output stage (BA1 and BA2) were then assembled by grouping the power cells into 150 μm pseudo-differential branches as in Fig. 2. The width of the PA blocks was chosen to maximize output power with good linearity. Differential topology was chosen for reliability and for the ease of power cell combination and drain supply feeding via center tap of the output balun. The CA can be

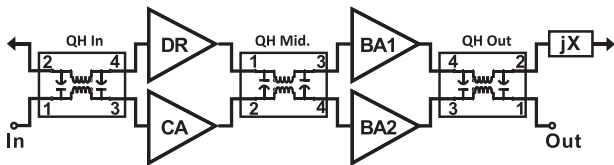


Figure 1. Block diagram of the integrated OLMBA.

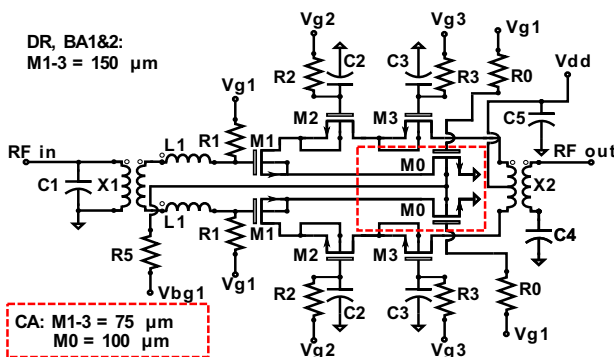


Figure 2. Schematic of a pseudo-differential PA building block.

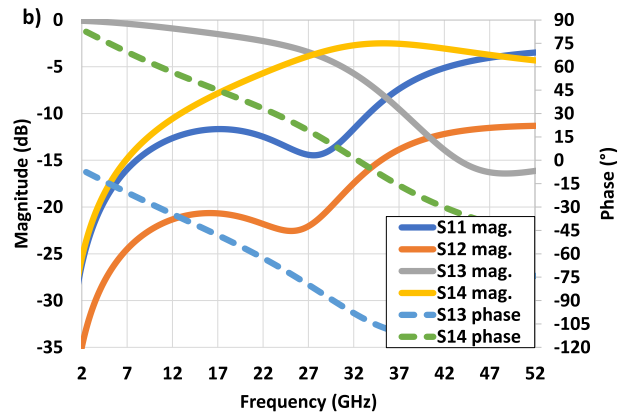
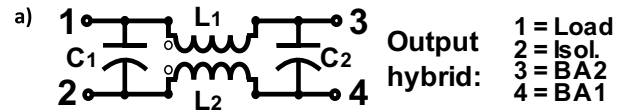


Figure 3. (a) Schematic of the transformer-based quadrature hybrid and (b) EM-simulated S-parameter plot.

much smaller than the rest of the amplifier blocks, since control signal levels of -10 dB compared to the main input signal can already cause significant load modulation [27]. CA has half of the width (75 μm per branch) compared to the other PA blocks and has a source degeneration transistor (M0, 100 μm) with back-gate bias option in addition to the normal gate bias V_{g1} , allowing better adjustment of its output power. CA output range spans from -27 dB to -4 dB, compared to the driver amplifier output power, and it can be adjusted with 1–2 dB steps. All of the PA blocks follow the same principle; the input matching and transformation from single-ended to pseudo-differential mode is done with a stacked transformer. On the output side, the power matching and transformation from pseudo-differential to single-ended is implemented with a center-tapped transformer, where the center tap functions as the drain bias line.

Quadrature hybrid

$$Y_{Qhyb} = \begin{bmatrix} \frac{1}{Z_{C1}} + \frac{Z_{L2}}{Z_{L1}Z_{L2} - Z_M^2} & -\frac{1}{Z_{C1}} - \frac{Z_M}{Z_{L1}Z_{L2} - Z_M^2} & -\frac{Z_{L2}}{Z_M} & \frac{Z_M}{Z_{L1}Z_{L2} - Z_M^2} \\ -\frac{1}{Z_{C1}} - \frac{Z_M}{Z_{L1}Z_{L2} - Z_M^2} & \frac{1}{Z_{C1}} + \frac{Z_{L2}}{Z_{L1}Z_{L2} - Z_M^2} & \frac{Z_{L2}}{Z_M} & -\frac{Z_M}{Z_{L1}Z_{L2} - Z_M^2} \\ -\frac{Z_{L2}}{Z_M} & \frac{Z_{L2}}{Z_M} & \frac{1}{Z_{C2}} + \frac{Z_{L1}}{Z_{L1}Z_{L2} - Z_M^2} & -\frac{1}{Z_{C2}} - \frac{Z_M}{Z_{L1}Z_{L2} - Z_M^2} \\ \frac{Z_M}{Z_{L1}Z_{L2} - Z_M^2} & -\frac{Z_M}{Z_{L1}Z_{L2} - Z_M^2} & -\frac{1}{Z_{C2}} - \frac{Z_M}{Z_{L1}Z_{L2} - Z_M^2} & \frac{1}{Z_{C2}} + \frac{Z_{L1}}{Z_{L1}Z_{L2} - Z_M^2} \end{bmatrix} \quad (1)$$

The quadrature hybrids in this work are based on a transformer tipped on its side. The coupling is further adjusted with capacitors. Benefits in utilizing transformer-based quadrature hybrids, as opposed to transmission line-based coupler implementations, are compact size and straightforward design approach. Figure 3 shows the quadrature hybrid schematic and frequency response. The general form of the resulting network is shortest to illustrate with a Y-parameter matrix (1). Z_{L1} , Z_{L2} , and Z_M in Equation (1) are the impedances of the primary side, secondary side, and mutual inductance, respectively. Z_{C1} and Z_{C2} correspondingly are impedances of the tuning capacitors. When the Y-parameter matrix is converted to the S-parameter matrix and we assume that the quadrature hybrid is symmetric ($L_1 = L_2$ and $C_1 = C_2$),

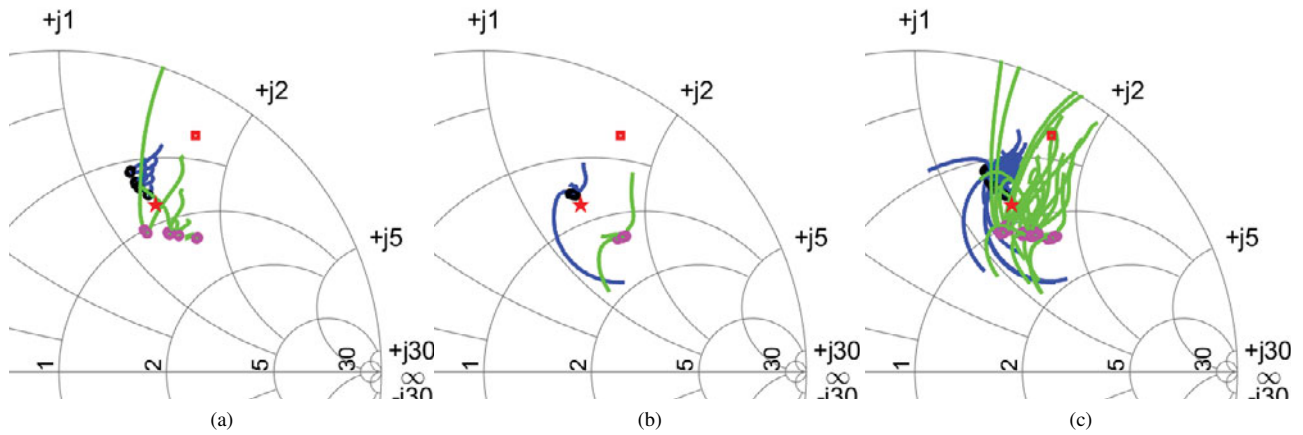


Figure 4. Illustration of load modulation behavior during power sweep depending on (a) DR and CPA bias settings, (b) BA1 and BA2 bias settings, and (c) both utilized simultaneously. The bias settings were swept from 290 mV to 380 mV with 30 mV steps. CA back-gate bias was set to 1.5 V (resulting in $|\alpha|$ in the range of -10 to -7 dB.) Blue and green lines depict impedances in BA1 and BA2 75 μm power cell drain, respectively. Black and magenta circles indicate the endpoints of the power sweep. The red square indicates the optimal impedance for back-off efficiency and the red pentagram is the maximum power efficiency point.

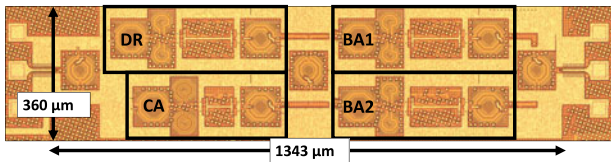


Figure 5. Micrograph of the fabricated PA.

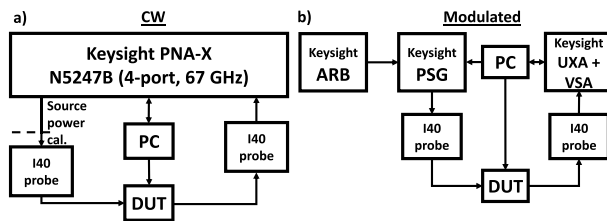


Figure 6. Block diagrams of (a) CW measurement setup and (b) modulated signal measurement setup.

then at a center frequency, the hybrid’s S-parameter matrix can be written as

$$S_{Q_{\text{hyb}}, f_c} = \begin{bmatrix} 0 & 0 & \frac{1}{\sqrt{2}} e^{j\phi_d} & \frac{1}{\sqrt{2}} e^{j\phi_c} \\ 0 & 0 & \frac{1}{\sqrt{2}} e^{j\phi_c} & \frac{1}{\sqrt{2}} e^{j\phi_d} \\ \frac{1}{\sqrt{2}} e^{j\phi_d} & \frac{1}{\sqrt{2}} e^{j\phi_c} & 0 & 0 \\ \frac{1}{\sqrt{2}} e^{j\phi_c} & \frac{1}{\sqrt{2}} e^{j\phi_d} & 0 & 0 \end{bmatrix}, \quad (2)$$

that is the hybrid provides good matching and isolation, and direct (S_{13}) and coupled (S_{14}) paths are equal in magnitude with phase offset relation $\phi_c = \phi_d + 90^\circ$.

Load modulation

As established in [27], the OLMBA load modulation is achieved by using the input quadrature hybrid isolation port (i.e. port 2 in Fig. 3, or correspondingly QH Mid. port 2 in Fig. 1) as a second input. The second input RF signal is referred to as the

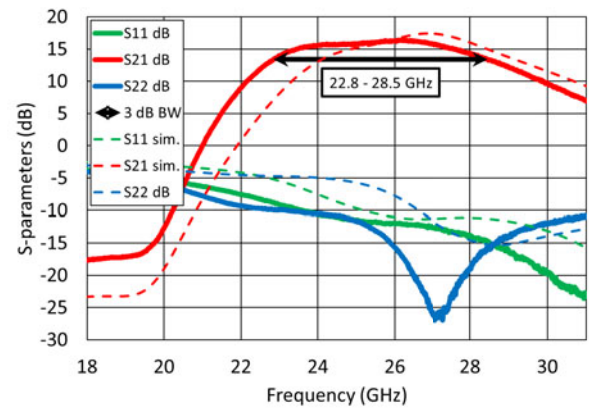


Figure 7. Measured and simulated S-parameters, with same bias settings as with 26 GHz results in Table 1.

control signal, and in Equations (3) and (4), it is expressed as relative term $\alpha = \frac{V_{in2}}{V_{in1}}$, where V_{in1} and V_{in2} refer to main and control signals, respectively. The control signal is amplified by the balanced PA pair and reflects back to their outputs from a reflective load placed to the output quadrature hybrid isolation port, causing load modulation.

$$\Gamma_{BA1} = \frac{(K_{BA2} - K_{BA1})j\Gamma_{iso} + \alpha(K_{BA2} + K_{BA1})\Gamma_{iso}}{(K_{BA2} - K_{BA1})j\Gamma_{iso}\Gamma_{PA} + 2K_{BA1} + \alpha((K_{BA2} + K_{BA1})\Gamma_{iso}\Gamma_{PA} + 2jK_{BA1})} \quad (3)$$

$$\Gamma_{BA2} = \frac{(K_{BA2} - K_{BA1})j\Gamma_{iso} + \alpha(K_{BA2} + K_{BA1})\Gamma_{iso}}{(K_{BA2} - K_{BA1})j\Gamma_{iso}\Gamma_{PA} + 2K_{BA2} + \alpha((K_{BA2} + K_{BA1})\Gamma_{iso}\Gamma_{PA} - 2jK_{BA2})} \quad (4)$$

In this work, the control signal is generated by dividing it from the main signal input with a quadrature hybrid (QH In in Fig. 1)

Table 1. Measurement results using CW and modulated signals

	Frequency (GHz)			
	24	26	27	29
I_{dQ} (mA)	63.3	55.1	54.7	89
Gain (dB)	15.9	16.6	15.4	15.9
P_{sat} (dBm)	19.6	19.5	19.2	18.7
PAE/DE _{max} (%)	15.8/21.6	15.7/24.8	13.9/19	11.4/16.6
P_{1dB} (dBm)	19.3	18.3	18.3	17.8
PAE/DE at 6 dB BO from P_{1dB} (%)	7/9.4	6.8/10.9	6.7/9.2	4.4/6.6
AM-PM at P_{1dB} (°)	3.8	2.2	2.3	7.2
100 MHz 64-QAM 3GPP/NR FR2				
P_{avg} (dBm)	12.1	11.4	11.2	11.5
EVM (dB)	-23.8 (6.4%)	-24.0 (6.3%)	-24.3 (6.1%)	-22.9 (7.2%)
aACLR (dBc)	-28.1	-28.9	-28	-28.1
PAE/DE _{avg} (%)	5.7/7.8	5.6/9.3	5.6/7.7	4.3/6.7

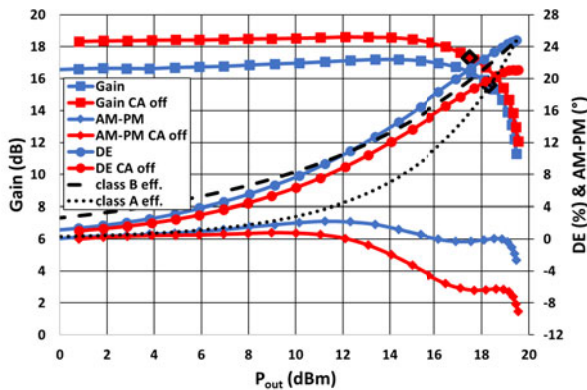


Figure 8. CW power sweep results measured at 26 GHz.

and amplifying it with the CA in a parallel path to the main signal driver amplifier (DR). This is to say that the control signal is fixed to -90° phase shift compared to the main path, except for any bias or frequency-dependent deviations in the phase relationship. The proposed OLMBA is capable of providing the $|\alpha|$ approximately up to -4 dB. The output quadrature hybrid has its isolation port terminated with a large capacitor, which is essentially a short circuit at the operating frequency. This control signal amplitude and phase and output isolation port load choice combination realizes load modulation between maximum and backed off power matching points as illustrated in Fig. 4. Both of the output stage-balanced PAs have their own bias controls, which enables additional degrees of freedom in the load modulation. The general form of the load modulation, expressed as reflection coefficients seen by BA1 and BA2 when antenna port load is assumed to be $Z_0 = 50\Omega$, is given in Equations (3) and (4), respectively. The equations are divided into two sections: only bias and isolation port load dependent and bias, control signal, and isolation port load dependent. K_{BA1} and

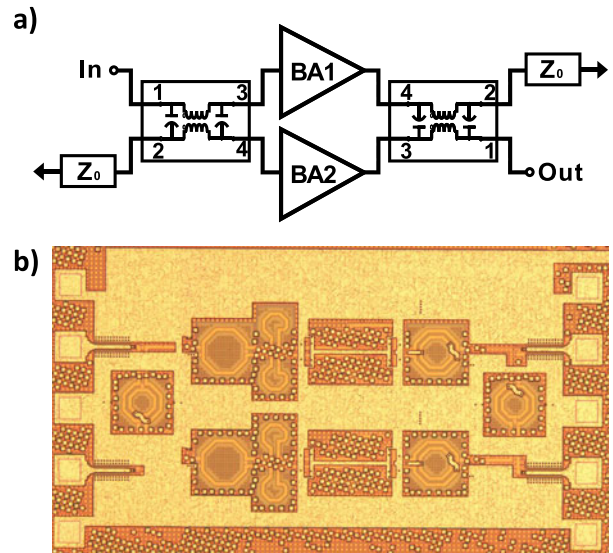


Figure 9. (a) Diagram and (b) micrograph of the stand-alone quadrature balanced PA.

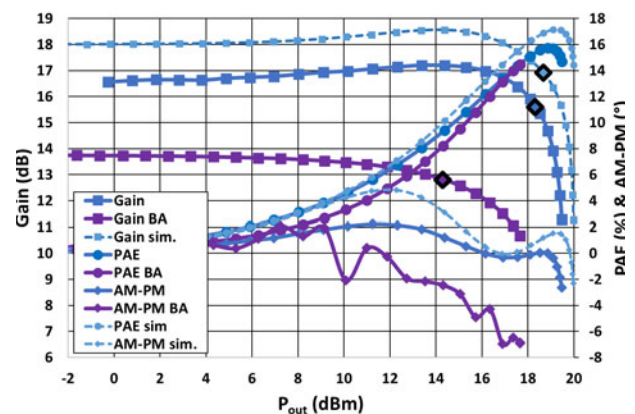


Figure 10. Simulated OLMBA results and comparison between OLMBA and stand-alone quadrature balanced PA power sweep measurement results, measured at 26 GHz. Light blue dashed lines indicate simulated OLMBA results and the diamond shapes indicate 1-dB compression points.

Table 2. CW measurements results comparison between stand-alone BA and OLMBA at 26 GHz

	BA	OLMBA
$P_{out, P_{3dB}}$ (dBm)	17.7	19.1
Gain (dB)	13.8	16.6
PAE _{P_{3dB}} (%)	14.5	15.7
PAE at 6 dB BO from P_{1dB} (%)	2.2	6.8
P_{1dB} (dBm)	14.3	18.3
AM-PM at P_{1dB} (°)	2.4	2.2

K_{BA2} denote the fundamental bias-dependent transconductances and Γ_{iso} denotes the output quadrature coupler reflective load. To be exact, the load modulation depends also on the S_{22} of the PAs, which is, in this case, assumed to be the same for both PAs and is denoted by Γ_{PA} .

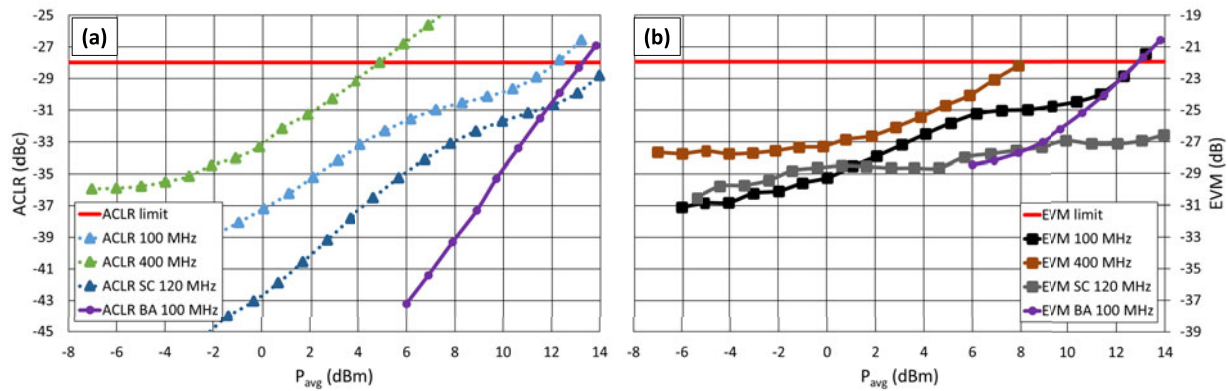


Figure 11. (a) ACLR and (b) EVM measurement results at 26 GHz.

The load modulation during a power sweep is illustrated with simulations in Fig. 4. The choice of $\Gamma_{iso} \approx -1$ and $\angle\alpha \approx -90^\circ$ causes the BA impedances to move both on a real and imaginary axes, as illustrated in Fig. 4(a). Initially, the control signal pushes the impedances higher toward the back-off efficiency matching point (red square), and they release during the power sweep toward the maximum power matching point (red pentagram). Black and magenta circles in Fig. 4 indicate the endpoints of the power sweep for BA1 (blue curves) and BA2 (green curves), respectively. Figure 4(b), on the other hand, illustrates load modulation during a power sweep, which can be achieved by setting BA1 and BA2 to uneven bias. When BA1 is at a higher bias, the load modulation moves roughly in a similar direction as with load modulation caused by the control signal. When BA2 dominates, the load modulation direction is the opposite. Lastly, Fig. 4(c) shows the ensuing load modulation when all controls are used.

Measurement results

Continuous wave measurements

A micrograph of the fabricated circuit is presented in Fig. 5. Continuous wave (CW) measurements were done using Keysight PNA-X network analyzer (N5247B, 4-port, 67 GHz) and FormFactor Infinity I40 probes. For the power sweeps, the power calibration plane was at the end of the cables and the probe losses (about 0.5 dB) were deducted from the results. The calibration was normalized using an external calibration substrate (Cascade P/N 101-190), and therefore the probe pads are included in the measurements. The chip had programmable DC biases for the lowest gates (V_{g1}) of the stacked transistors. Upper gate biases (V_{g2} and V_{g3}) were set to fixed values and generated with off-chip voltage supplies, so that none of the transistors would exceed maximum V_{ds} of 900 mV. The PA bias settings and the measurement equipment were controlled using MATLAB. Block diagram of the CW measurement setup is shown in Fig. 6(a).

Measured and simulated S-parameters are presented in Fig. 7. The measured frequency response (solid lines) has shifted lower compared to the simulated (dashed lines). This is dominantly because the whole structure was already demanding to simulate as a single EM-block, and because of that, the metal fills were not included in the simulations. The measured 3-dB bandwidth ended up spanning from 22.8 GHz to 28.5 GHz, with 26 GHz as the center frequency. S11 and S22 both remain below -10 dB throughout the operating range. S12 stays below -45 dB and is omitted for clarity.

Table 3. Modulated signal performance comparison between stand-alone BA and OLMBA at 26 GHz with 100 MHz 64-QAM OFDM signal

	BA	OLMBA
Performance at $P_{avg} = 12$ dBm		
EVM (dB)	-23.3 (6.9%)	-23.3 (6.9%)
ACLR (dBc)	-30.5	-28.2
PAE (%)	4.6	6.1
Performance at $P_{avg} = 9$ dBm		
EVM (dB)	-26.9 (4.5%)	-24.8 (5.7%)
ACLR (dBc)	-36.8	-30.3
PAE (%)	2.3	3.5

For the power sweeps, the biases of DR, CA, BA1 and BA2 were swept with a focus on finding the settings producing the high output 1-dB compression point (P_{1dB}) with minimal amplitude to phase modulation (AM-PM). The estimated bias range for the (V_{g1}) sweeps was from 290 to 380 mV, with cut-off voltage being at 200 mV and saturation voltage at 490 mV. Measurement results at different frequencies with their respective bias settings (for brevity expressed as the total drain current I_{dQ}) are listed in Table 1. Figure 8 shows an example of a power sweep at 26 GHz, where otherwise the same bias settings are compared with and without control amplifier contribution. When the control amplifier is on, which is the blue curves, we get some penalty in gain, but the compression point improves by one dB and AM-PM improves by five degrees. Additionally, the output stage drain efficiency improves by three percentage points. Figure 8 also contains normalized reference lines for ideal class A and B efficiencies. At 6 dB back-off from P_{1dB} , the efficiency is as good as with class B and 2.3 times better than class A.

The integrated OLMBA was compared to a stand-alone integrated quadrature balanced amplifier (BA) with 50 Ω loads at the isolation ports, as illustrated in Fig. 9(a). The micrograph of the BA PA is shown in Fig. 9(b). The stand-alone BA test circuit consists of BA1 and BA2 without a driving stage, fed and terminated with GSGSG pads. Power sweep results at 26 GHz are compared in Fig. 10 and in Table 2. Without driver amplifier, the measurement equipment source power was adequate to push the stand-alone BA only to 3 dB compression. However, 3 dB compression can be assumed close to saturation, and the comparison results indicate

Table 4. Comparison to the state-of-the-art

	This work		[31]	[25]	[26]	[32]
Technology	22 nm FDSOI		22 nm FDSOI	65 nm CMOS	28 nm CMOS	45 nm RFSOI
Architecture	OLMBA		Doherty	LMBA	LMBA	Doherty
Frequency (GHz)	26		28	33	36	32.5
Supply (V)	2.7		2.4	1.1	1	2 & 1
Gain (dB)	16.6		26.1	10	18	–
P_{sat} (dBm)	19.5		22.5	20	22.6	22
PAE _{max} (%)	15.7		28.5	23.3	32	40.5
$P_{1\text{dB}}$ (dBm)	18.3		21.1	–	19.6	21.5
Modulation scheme	OFDM 64-QAM	SC 64-QAM	SC 64-QAM	SC 64-QAM	SC 64-QAM	OFDM 64-QAM
Bandwidth (MHz)	100	4x100	120	–	–	200
Data rate (Gb/s)	0.492	1.97	0.6	2.4	0.6	6
P_{avg} (dBm)	11.4	4.9	14	10.9	11.8	10.6
EVM (dB)	–24	–24.7	–26.6	–25.1	–25.1	–27
ACLR (dBc)	–28.9	–28	–28.8	–28	–28.2	–29
PAE _{avg} /DE _{avg} (%)	5.6/9.3	1.7/3.1	8.8/13.7	9.2/–	11.6/–	–/12.1
$\frac{\text{PAE}_{\text{avg}}}{\text{PAE}_{\text{max}}}$	0.36	0.11	0.56	0.32	0.41	0.32 (DE)
Area (mm ²)	0.484		0.2	1.47	1.44	0.62

that OLMBA is able to squeeze more power out, with better maximum and backed-off efficiency. PNA-X differential IQ mode was used in the additional BA measurements and that causes some phase fluctuation in the AM-PM results of the stand-alone BA. Figure 10 also contains simulated results of the OLMBA, which show roughly 1 dB more gain and slightly higher PAE. Overall, the simulations match well with the measurements.

Modulated measurements and comparison to the state-of-the-art

Modulated measurements were conducted using the same bias settings that were used with continuous wave measurements presented in the previous section. Three waveforms were chosen as test signals: 100 and 400 MHz 64-QAM 3GPP/NR frequency range 2 (FR2) waveforms (10.9 dB peak to average power ratio with 1e-3 peak probability) and a 0.6 Gb/s (120 MHz) single carrier (SC) 64-QAM signal (0.35 roll-off factor). The signals were generated with Keysight arbitrary waveform generator (Keysight M8190A) and with Keysight programmable signal generator (Keysight E8257D). The output channel power and adjacent channel leakage ratio (ACLR) were measured with Keysight UXA (N9040B) signal analyzer. Error vector magnitude (EVM) was captured using vector signal analyzer (VSA) software. Same as with previous measurements, the sweeps were controlled and data were captured with MATLAB. Measurement setup EVM and ACLR before the PA under test were measured to be 2.3% (–32.8 dB) and –42 dBc, respectively. Block diagram of the modulated measurement setup is shown in Fig. 6(b).

3GPP defined limits for ACLR and EVM were used as threshold values for reporting the average output power with modulated signals. The limits are –28c dB and 8% (–21.9 dB) for ACLR and EVM, respectively [5]. ACLR measurements with three different signals are presented in Fig. 11(a) and EVM sweeps in Fig. 11(b).

ACLR can be seen to be more limiting, especially with 400 MHz signal. Measured at 26 GHz, the PA reaches 11.4 dBm P_{avg} with 100 MHz 64-QAM OFDM signal and 4.9 dBm with 400 MHz 64-QAM OFDM signal. With SC signal, OLMBA achieves 14 dBm P_{avg} with good margin of linearity. Results with 100 MHz OFDM signal are also summarized in Table 1, where the PA shows steady performance throughout the tested frequencies, with average power fulfilling the linearity specifications staying within 1 dB. Figure 11 contains also stand-alone BA measurement results with 100 MHz 64-QAM OFDM signal for reference. Stand-alone BA can be seen to have better linearity in deep back-off but reaches the same output power with the linearity threshold. The differences between BA and OLMBA modulated performance are further examined in Table 3. The comparison is done at two average output power levels set 3 dB apart. OLMBA provides better efficiency in backed-off power levels.

Measurement results at 26 GHz are compared to other state-of-the-art advanced PA solutions in Table 4. With CW results, the proposed PA delivers comparable output power, gain, and output compression point. With modulated signals, the proposed PA provides comparable results, especially considering that most of the others were not tested using 5G NR signals. It should be noted that SC 64-QAM signal can have 4–5 dB lower PAPR compared to the OFDM 64-QAM used in this work [12, 32].

Conclusion

This paper presented a fully integrated PA demonstrating OLMBA architecture at 3GPP/NR FR2 frequency range 24.25–29.5 GHz. Differing from the previously established theory of operation, the design part included also the effect of biasing the output stage asymmetrically. The prototype was fabricated with GlobalFoundries 22 nm complementary metal oxide semiconductor (CMOS) FDSOI. The PA was tested with CW measurements

and several modulated waveforms, including demanding 5G signals. Measured at 26 GHz, the PA achieves P_{sat} , gain, PAE, and $P_{1\text{dB}}$ of 19.5 dBm, 16.6 dB, 15.6%, and 18.3 dBm, respectively. With high dynamic range 100 and 400 MHz 64-QAM 3GPP/NR OFDM signals, the PA reaches 11.4 and 4.9 dBm P_{avg} with -28 dB and 8% (-21.9 dB) as ACLR and EVM specifications, respectively. With 0.6 Gb/s SC 64-QAM, the PA reaches 14 dBm P_{avg} . The proposed PA was also compared to a stand-alone quadrature-balanced PA test structure, and the measurements showed that the OLMBA reached the same output power within the linearity specifications but with better efficiency. Compared to other load-modulated Ka-band PAs, the prototype delivers similar or better performance with a new architecture, showing that it is a promising candidate for 5G mmWave use.

Acknowledgements. The authors would like to thank GlobalFoundries for providing silicon fabrication through the 22FDX University program. Jere Rusanen would like to thank Seppo Säynäjäkangas Science Foundation and Foundation of Riitta and Jorma J. Takanen for personal grants.

Funding statement. This research has been financially supported by Infotech Oulu and Academy of Finland research projects MIMEPA (grant 323779) and 6G Flagship (grant 346208).

Competing interests. The authors declare none.

References

1. **Nokia Bell Labs** (2019) Industrial IoT Networks: 5G transforming industry verticals. <https://onestore.nokia.com/asset/202286> (accessed 26 May 2023).
2. **Ericsson ConsumerLab** (2019) 10 hot consumer trends 2030. <https://www.ericsson.com/4ae13b/assets/local/reports-papers/consumerlab/reports/2019/10hctreport2030.pdf> (accessed 26 May 2023).
3. **Shafi M, Tataria H, Molisch AF, Tufvesson F and Tunnicliffe G** (2020) Real-time deployment aspects of C-band and millimeter-wave 5G-NR systems. In *ICC 2020–2020 IEEE International Conference on Communications (ICC)*. Dublin, Ireland, IEEE, pp. 1–7. doi:10.1109/ICC40277.2020.9148902.
4. **Latva-aho M** (2019) Key drivers and research challenges for 6G ubiquitous wireless intelligence. Oulun yliopisto. <http://urn.fi/urn:isbn:9789526223544> (accessed 26 May 2023).
5. **3 GPP** (2021) Base station (BS) radio transmission and reception, 3rd Generation Partnership Project (3GPP) Technical Specification (TS) 38.104, version 17.2.0, https://www.3gpp.org/ftp/Specs/archive/38_series/38.104/38104-h20.zip (accessed 26 May 2023).
6. **Sadhu B, Gu X and Valdes-Garcia A** (2019) The more (antennas), the merrier: A survey of silicon-based mm-Wave phased arrays using multi-IC scaling. *IEEE Microwave Magazine* **20**(12), 32–50.
7. **Roh W, Seol J, Park J, Lee B, Lee J, Kim Y, Cho J, Cheun K and Aryanfar F** (2014) Millimeter-wave beamforming as an enabling technology for 5G cellular communications: Theoretical feasibility and prototype results. *IEEE Communications Magazine* **52**(2), 106–113.
8. **Han S, Chih-Lin I, Xu Z and Rowell C** (2015) Large-scale antenna systems with hybrid analog and digital beamforming for millimeter wave 5G. *IEEE Communications Magazine* **53**(1), 186–194.
9. **Tuovinen T, Tervo N and Pärssinen A** (2017) Analyzing 5G RF system performance and relation to link budget for directive MIMO. *IEEE Transactions on Antennas and Propagation* **65**(12), 6636–6645.
10. **Rikkinen K** (2020) THz radio communication: Link budget analysis toward 6G. *IEEE Communications Magazine* **58**(11), 22–27.
11. **Camarchia V, Quaglia R, Piacibello A, Nguyen DP, Wang H and Pham A-V** (2020) A review of technologies and design techniques of millimeter-wave power amplifiers. *IEEE Transactions on Microwave Theory and Techniques* **68**(7), 2957–2983. doi:10.1109/TMTT.2020.2989792
12. **Wang H, Asbeck PM and Fager C** (2021) Millimeter-wave power amplifier integrated circuits for high dynamic range signals. *IEEE Journal of Microwaves* **1**(1), 299–316. doi:10.1109/JMW.2020.3035897
13. **Tervo N** (2021) Digital predistortion of phased-array transmitter with shared feedback and far-field calibration. *IEEE Transactions on Microwave Theory and Techniques* **69**(1), 1000–1015. doi:10.1109/TMTT.2020.3038193
14. **Asbeck PM, Rostomyan N, Özen M, Rabet B and Jayamon JA** (2019) Power amplifiers for mm-Wave 5G applications: Technology comparisons and CMOS-SOI demonstration circuits. *IEEE Transactions on Microwave Theory and Techniques* **67**(7), 3099–3109. doi:10.1109/TMTT.2019.2896047
15. **Jayamon JA, Buckwalter JF and Asbeck PM** (2016) Multigate-cell stacked FET design for millimeter-wave CMOS power amplifiers. *IEEE Journal of Solid-State Circuits* **51**(9), 2027–2039. doi:10.1109/JSSC.2016.2592686
16. **Park B** (2016) Highly linear mm-Wave CMOS power amplifier. *IEEE Transactions on Microwave Theory and Techniques* **64**(12), 4535–4544. doi:10.1109/TMTT.2016.2623706
17. **Kim B, Moon K, Jeong D, Kim S and Shin J** (2017) Linear PA at mm-Wave band for 5G application. In *2017 10th Global Symposium on Millimeter-Waves*. Hong Kong, China, IEEE, pp. 80–82. doi:10.1109/GSMM.2017.7970326
18. **Shakib S, Park H-C, Dunworth J, Aparin V and Entesari K** (2016) 20.6 A 28GHz efficient linear power amplifier for 5G phased arrays in 28nm bulk CMOS. In *2016 IEEE International Solid-State Circuits Conference (ISSCC)*. San Francisco, CA, USA, IEEE, pp. 352–353. doi:10.1109/ISSCC.2016.7418052.
19. **Fang X, Xia J and Boumaiza S** (2020) A 28-GHz beamforming Doherty power amplifier with enhanced AM-PM characteristic. *IEEE Transactions on Microwave Theory and Techniques* **68**(7), 3017–3027. doi:10.1109/TMTT.2020.2968318
20. **Wang F and Wang H** (2020) 24.1 A 24-to-30GHz Watt-level broadband linear Doherty power amplifier with multi-primary distributed-active-transformer power-combining supporting 5G NR FR2 64-QAM with $<19\text{ dBm}$ average Pout and $<19\%$ average PAE. In *2020 IEEE International Solid-State Circuits Conference – (ISSCC)*. San Francisco, CA, USA, IEEE, pp. 362–364. doi:10.1109/ISSCC19947.2020.9063146
21. **Rostomyan N, Özen M and Asbeck P** (2018) 28 GHz Doherty power amplifier in CMOS SOI with 28% back-off PAE. *IEEE Microwave and Wireless Components Letters* **28**(5), 446–448. doi:10.1109/LMWC.2018.2813882
22. **Wang F, Li T-W, Hu S and Wang H** (2019) A super-resolution mixed-signal Doherty power amplifier for simultaneous linearity and efficiency enhancement. *IEEE Journal of Solid-State Circuits* **54**(12), 3421–3436. doi:10.1109/JSSC.2019.2937435
23. **Maroldt S, and Ercoli M** (2017) 3.5 GHz ultra-compact GaN class-E integrated Doherty MMIC PA for 5G massive-MIMO base station applications. In *12th European Microwave Integrated Circuits Conference (EuMIC)*. Nuremberg, Germany, IEEE, pp. 196–199.
24. **Sheppard DJ, Powell J and Cripps SC** (2016) An efficient broadband reconfigurable power amplifier using active load modulation. *IEEE Microwave and Wireless Components Letters* **26**(6), 443–445. doi:10.1109/LMWC.2016.2559503
25. **Chappidi CR, Sharma T, Liu Z and Sengupta K** (2020) Load modulated balanced mm-Wave CMOS PA with integrated linearity enhancement for 5G applications. In *2020 IEEE/MTT-S International Microwave Symposium (IMS)*. Los Angeles, CA, USA, IEEE, pp. 1101–1104. doi:10.1109/IMS30576.2020.9224038
26. **Qunaj V and P Reynaert** (2021) 26.2 A Doherty-like load-modulated balanced power amplifier achieving 15.5 dBm average Pout and 20% average PAE at a data rate of 18Gb/s in 28nm CMOS. In *2021 IEEE International Solid-State Circuits Conference (ISSCC)*. San Francisco, CA, USA, IEEE, pp. 356–358. doi:10.1109/ISSCC42613.2021.9365966
27. **Collins DJ, Quaglia R, Powell JR and Cripps SC** (2020) The orthogonal LMB: A novel RFPA architecture with broadband reconfigurability. *IEEE Microwave and Wireless Components Letters* **30**(9), 888–891. doi:10.1109/LMWC.2020.3010817

28. **Quaglia R, Powell JR, Chaudhry KA and Cripps SC** (2022) Mitigation of load mismatch effects using an orthogonal load modulated balanced amplifier. *IEEE Transactions on Microwave Theory and Techniques* **70**(6), (June) 3329–3341. doi:10.1109/TMTT.2022.3167414
29. **Rusanen J, Sethi A, Tervo N, Rahkonen T, Parssinen A, Kiuru V, Aikio JP** (2022) Ka-band orthogonal load-modulated balanced amplifier in 22 nm CMOS FDSOI. In *2022 17th European Microwave Integrated Circuits Conference (EuMIC)*. Milan, Italy, IEEE, pp. 161–164. doi:10.23919/EuMIC54520.2022.9923540
30. **Ong SN, Lehmann S, Chow WH, Zhang C, Schippel C, Chan LHK, Andee Y, Hauschildt M, Tan KKS, Watts J, Lim CK, Divay A, Wong JS, Zhao Z, Govindarajan M, Schwan C, Huschka A, Bcllaouar A, LOo W, Mazurier J, Grass C, Taylor R, Chew KWL, Embabi S, Workman G, Pakfar A, Morvan S** (2018) A 22nm FDSOI technology optimized for RF/mmWave applications, In *2018 IEEE Radio Frequency Integrated Circuits Symposium (RFIC)*. Philadelphia, PA, USA, IEEE, pp. 72–75. doi:10.1109/RFIC.2018.8429035
31. **Zong Z** (2021) A 28-GHz SOI-CMOS Doherty power amplifier with a compact transformer-based output combiner. *IEEE Transactions on Microwave Theory and Techniques* **69**(6), 2795–2808. doi:10.1109/TMTT.2021.3064022
32. **Huang T-Y, Mannem NS, Li S, Jung D, Huang M-Y and Wang H** (2021) 26.1 A 26-to-60GHz continuous coupler-Doherty linear power amplifier for over-an-octave back-off efficiency enhancement. In *2021 IEEE International Solid-State Circuits Conference (ISSCC)*. San Francisco, CA, USA, IEEE, pp. 354–356. doi:10.1109/ISSCC42613.2021.9365858



Jere Rusanen received his M.Sc. (Tech.) degree in electrical engineering in 2014. Currently, he works part-time as a doctoral researcher in University of Oulu and as a technical leader in radio system architecture team at Nokia. During 2014–2019, he worked as an antenna engineer at Nokia, Oulu. His research interests include integrated millimeter wave power amplifiers.



Alok Sethi received the M.Sc. degree in wireless communications engineering from the University of Oulu, Oulu, Finland, in 2013, where he is currently pursuing the Ph.D. degree.



Nuutti Tervo received the B.Sc. (Tech.), M.Sc. (Tech.), and D.Sc. (Tech.) degrees from the University of Oulu, Oulu, Finland, in 2014 and 2022, all with distinctions. His doctoral dissertation research focused on nonlinearity and linearization of millimeter-wave beamforming transceivers. Since 2022, he has been a post-doctoral researcher at the Centre for Wireless Communications – Radio Technologies (CWC-

RT) research unit at the University of Oulu. He has a strong background in wireless communications, including radio frequency (RF), radio channel

modeling, signal processing, and system-level analysis. Around those topics, he has already authored or coauthored more than 60 international journal and conference papers and he holds several patents. In 2019, he was a recipient of the Young Scientist Award of the URSI XXXV Finnish Convention on Radio Science, Tampere, and in 2020, he co-authored the paper that won the 50th EuMC Microwave Prize 2020, Utrecht, Netherlands.



Veeti Kiuru received his M.Sc. degree on electrical engineering from University of Oulu in 2020. Currently, he is working in Sony as a physical layer and L1 layer firmware engineer. His interests include millimeter wave integrated circuits, PCB design, and repairing and FW/SW development in the area of 5G.



Timo Rahkonen was born in Jyväskylä, Finland, 1962. He received his Diploma Engineer, Licentiate, and Doctor of Technology degrees in 1986, 1991, and 1994, respectively, in University of Oulu, Finland. Currently, he is a professor in circuit theory and circuit design in University of Oulu, Oulu, Finland, conducting research on linearization and error correction techniques for RF power amplifiers and A/D and D/A converters.



Aarno Pärssinen received D.Sc. degree from Helsinki University of Technology in 2000. From 1994 to 2000, he was with Electronic Circuit Design Laboratory, Helsinki University of Technology, Finland, working on direct conversion receivers. In 1996, he was a Research Visitor at the University of California at Santa Barbara. From 2000 to 2011, he was with Nokia Research Center. During 2009–2011, he served as a member of Nokia CEO Technology Council. From 2011 to 2013, he was at Renesas Mobile Corporation working as a Distinguished Researcher and RF Research Manager. From October 2013 to September 2014, he was an Associate Technical Director at Broadcom. Since September 2014, he has been with University of Oulu, Centre for Wireless Communications, Oulu, Finland, where he is currently a Professor. His research interests include wireless systems and transceiver architectures for wireless communications with special emphasis on the RF and analog integrated circuit and system design.



Janne P. Aikio was born in Haukipudas, Finland, in 1977. He received the M.Sc. and Ph.D. degrees in electrical engineering from the University of Oulu, Oulu, Finland, in 2002 and 2007, respectively. He is currently a Postdoctoral Researcher with the University of Oulu. His technical interests lie in the field of millimeter-wave integrated power amplifiers and modeling and analysis of distortion of RF power amplifiers.